RESEARCH ARTICLE

MATERIALS SCIENCE

Superior microwave shielding modulation based on rapidly prepared graphene metasurface

Pengfei Chen, 1,2,3,# Xinrui Yang, 1,2,# Yifan Chang, 1,2 Wei Qian, 2,4 Huaqiang Fu, 1,2 Wenxiang Xu, 2 Lin Ren, 2,5 Zhe Wang, 4,* Haoran Zu, 2,6,* Dingsheng Wang 7 and Daping He 1,2,3,*

¹School of Materials Science and Engineering, Wuhan University of Technology, Wuhan 430070, China;

²Hubei Engineering Research Center of Radio Frequency Microwave Technology and Application, School of Physics and Mechanics, Wuhan University of Technology, Wuhan 430070, China;

³State Key Laboratory of Silicate Materials for Architectures, Wuhan University of Technology, Wuhan 430070, China;

⁴State Key Laboratory of Advanced Technology for Materials Synthesis and Processing, Wuhan University of Technology, Wuhan 430070, China;

⁵Hubei Longzhong Laboratory, Wuhan University of Technology Xiangyang Demonstration Zone, Xiangyang 441000, China;

⁶School of Information Engineering, Wuhan University of Technology, Wuhan 430070, China

⁷Department of Chemistry, Tsinghua University, Beijing 100084, China

*Corresponding authors. E-mail: <u>wangzhe0614@whut.edu.cn</u>; <u>zuhr@whut.edu.cn</u>; hedaping@whut.edu.cn

#Equally contributed to this work.

ABSTRACT

Active manipulation of electromagnetic wave jamming is a critical challenge for next-generation adaptive electronics. Electrical conductivity-tunable porous materials have been developed, but encountering the challenge of constrained modulation range and large thickness. Herein, we report a method for modulating the shielding efficiency of microwaves based on micrometer-thick graphene metasurface. The continuous modulation between wave transmission and shielding in an ultra-wide range of 9.66%–99.78% is achieved, due to the remarkable anisotropy of wave-induced electron oscillation. By rotating the metasurface, wherein alignment of the periodically arranged graphene strips with the incident electric field enhances electron oscillations and boosts secondary radiation, thus significantly improving shielding efficiency. Notably, the metasurface achieves facile preparation and open-air processability utilizing laser-induced ultrafast kinetics, facilitating its application in advanced smart electromagnetic devices. Finally, we demonstrate its potential in a novel paradigm for data electromagnetic encryption.

Keywords: electromagnetic shielding modulation, laser-induced graphene, metasurface, rapid preparation

INTRODUCTION

Electromagnetic shielding materials, including metals, transition metal carbides, and carbon materials, have been widely developed for reducing electromagnetic interference (EMI). However, the inherent fixed physicochemical properties of these materials limit their ability to meet the evolving demands of highly integrated and adaptive smart electronics [1-4]. It is highly desired to develop next-generation smart EMI shielding materials with tunable EMI shielding efficiency in response to real-time environmental changes or artificially imposed conditions. This tunability, however, presents challenges in material structure design for synchronously ensuring precise properties' control and cycle stability.

Five primary regulation strategies have been identified for dynamically modulating EMI shielding efficiency: electrochemical potential [1], mechanical deformation [5-7], rotation [8,9], humidity [10], and temperature [11]. For instance, Han et al. employed MXene films to electrochemically drive ion intercalation/de-intercalation with the expansion and shrinkage of MXene layer spacing [1], demonstrating a novel approach for controlling electromagnetic waves. However, the modulation range (94.31%–99.95%) is typically constrained, while the long preparation time (> 44 hours) and complex fabrication process of MXene limit the scalability of this strategy. Liu et al. prepared a wood-derived carbon/XC-72 nanoparticle aerogel with compression-driven electrical tunability [2]. The compression enables the carbon nanoparticles to establish highly conductive pathways, thereby activating EMI shielding performance. But the excessive thickness of 2-7 cm hinders its application in integrated electronics. It can be seen that the key of current technical route is to first construct nanostructures and subsequently change nanomaterial blocks' structure through various external physical fields, thereby affecting conductivity and EMI shielding efficiency. The current challenges of stringent synthesis conditions, prolonged synthesis time and excessive thickness hinder scalable applications. Thus, it is urgent to develop easy-prepared yet large-tunable-range EMI shielding thin film material.

Generally, the EMI shielding efficiency of a material is positively correlated to its electrical conductivity, so highly conductive materials are preferred [12-15]. However, materials capable of superior electromagnetic shielding modulation, achieving wave transmission/shielding (On/Off) switching, requires nearly no/highly conductive in two states.

This will even put forward higher requirements for nanostructure construction in thin film [16-20]. As such, constructing an electromagnetic metasurface to achieve tunable reflection and adsorption of electromagnetic wave is an indispensable approach. Both high conductivity and accurate patterning are indispensable, because they jointly determine the modulation capability. However, metasurface preparation methods, such as screen printing and ink printing, encounter the problem of balancing the viscosity and electrical conductivity of printing inks, thus leading to compromised On/Off switchable performance. To the best of our knowledge, none of the existing EMI shielding thin film material fully meet the above-mentioned requirements. The design and preparation of such smart EMI shielding material is a notable technological challenge.

Here, we report a laser-induced graphene (LIG) based smart metasurface with superior EMI shielding modulation capability. The regulation range of EMI shielding efficiency can be unprecedentedly broadened to 9.66% (On state)–99.78% (Off state) due to the anisotropic wave-induced electron oscillation, which can be strongly activated when the strip-arranged graphene aligns with the incident electric field, thereby enhancing secondary radiation opposite to incident one. Remarkably, the metasurface is rapidly prepared in a single step with improved patterning accuracy, and a 5×5 cm² surface can be produced in just 5 minutes at room temperature and ambient pressure. The facile fabrication approach enhances its practical applicability. Finally, we demonstrate its substantial role in a novel paradigm for data encoding and encryption. The availability of this metasurface, featuring promising EMI shielding modulation capability, lays the groundwork for future advancements in intelligent electromagnetic devices and systems.

RESULTS AND DISCUSSION

Rotation modulated EMI shielding with LIG based metasurface

To realize the rapid preparation of EMI shielding metasurface under ambient temperature and atmospheric conditions, laser-induced technology was adopted. As depicted in Figure 1a1, a periodically strip-arranged metasurface is designed and fabricated to achieve tunable electromagnetic shielding performance. An infrared laser serves as the light source, converting polyimide (PI) into graphene on the PI film surface through processes of reflection, focusing, and scanning. PI can effectively absorb the infrared laser with a wavelength of 1064 nm [21], inducing instantaneous photochemical reactions (Note SI), including bond dissociation [22,23], carbonization [24], and graphitization [25,26]. After stripping off the upper layer, the gully structure on surface and internal of LIG exhibit a distinct porous morphology (Figures 1a2 and S1), attributed to the ultrafast release of significant amounts of CO₂ and N₂ gases generated during the laser-induced rapid bond-dissociation and carbonization of PI molecules (Figure 1a₃). Notably, the high-precision patterning in LIG technology remains a challenge due to the photothermal effect induced by the high-energy pulse, which extends beyond the irradiated area, leading to reduced patterning accuracy, as shown in Figure S2. Through repeated experimentation (Figures S3 and S4), we achieved enabled the controllable and reproducible achievement of high-precision processing, with a minimum line width and inter-line gap of ~31.8 μm and ~7.2 µm, respectively (Figure 1b). Based on these, complex and high-resolution LIG patterning can be realized, as exemplified by the successful fabrication of a Chinese knot-shaped LIG with dimensions of ~2.75 × 2.85 cm² (Figures 1b and S5). Compared to previously reported works, this work demonstrates superior patterning accuracy (Table S1, Figure S6). This lays a critical foundation for the fabrication of EMI shielding metasurfaces, as the LIG widths and gap widths are pivotal in determining the electromagnetic modulation performance (Note S2).

Figure 1c shows a photograph of the strip-arranged LIG metasurface sample, demonstrating exceptional flexibility while maintaining structural integrity after bending and twisting. This design facilitates the modulation of wave-induced electron oscillation strength

and secondary radiation, thereby enabling dynamic control of the interaction between electromagnetic waves and the shielding material. As α increases from 0° to 90°, the penetrating electromagnetic field progressively increases in intensity, transitioning through the "Off", "Semi", and "On" states, respectively (Figure 1d), exhibiting remarkable EMI shielding switching characteristics. The tunable range is a critical metric for assessing dynamic wave control performance, with the surface exhibiting distinctly different electromagnetic responses (wave transmission/shielding) in the On/Off states. In this context, the widest reported tunable range of EMI shielding efficiency (11.5%-99.8%) and tremendously shortened synthesis duration of 5 minutes have been achieved (Figure 1e, **Table S2**). Notably, synthesis times are reported as the sum of individual process durations, excluding inter-step intervals. While various factors influence synthesis duration, we present these data as a qualitative reference, underscoring the urgency of developing practical, industrially relevant synthesis methods for electromagnetic functional thin films. Shielding efficiency (measured in %) is considered a more appropriate performance metric for On/Off switchable EMI shielding modulation than SE (measured in dB), as SE values, processed mathematically to describe high shielding efficiency (> 90%) but fail to intuitively reflect On-state performance (Note S3). Notably, the characteristics of single-step patterning fabrication, easy control, reversibility, and rotation modulated switching facilitate its critical prospect in information coding and encryption (Figure 1f).

Laser-focused/defocused-dependent properties of LIG

Compared to conventional heating technologies [27], laser processing exhibits distinct advantages, including higher energy density, faster heating rates. Notably, the thermogravimetric (TG) analysis (**Figure S7**) reveals that PI undergoes complete decomposition at approximately 700°C with a heating rate of 5 °C min⁻¹ under atmospheric conditions. In contrast, the temperature required for PI carbonization and C-sp³ to C-sp² transformation significantly exceeds 700°C in LIG fabrication. This is supposed to be the results of unique fast laser pulses, which lead to an instantaneous photothermal effect, enabling rapid surface heating and cooling (**Figure S7**). Simultaneously, the laser pulse induces a photoetching effect, applying stress to the PI surface [28,29], which facilitates the

rupture of chemical bonds within PI molecules. Figure 2a presents a schematic illustrating the difference between laser-focused and laser-defocused scanning on PI surface. The irradiated area of defocused laser is larger than that of focused laser, leading to decreased power density and larger repeatedly scanned region. Figure 2b shows that the thickness of LIG prepared by laser-focused scanning (F-LIG) and laser-defocused scanning (DF-LIG) increases nearly linearly with power, as more PI molecules react with increased power. The electrical conductivity of LIG initially increases and then decreases with increasing pulse power (Figure 2c). The initial increase is attributed to higher induced energy, which promotes the transformation of amorphous carbon with poor conductivity into stacked graphene sheets with improved conductivity. However, beyond a threshold power, excessive energy leads to an excessively rapid gas-release-rate, resulting in the formation of more internal voids and degradation of surface morphology [26,30], thereby negatively affecting the overall conductivity. Specifically, DF-LIG exhibits better conductivity than F-LIG, owing to fewer defects and a more continuous surface morphology. Moreover, a laser power of 3 W provides insufficient energy to form LIG, resulting in almost no change on PI surface. A laser power of 8 W is of limited practical value, as the excessive energy results in substantial deformation of prepared film (Figure S8) and causes significant measurement errors in both thickness and conductivity. In this work, subsequent EMI shielding related tests will focus on samples prepared under laser powers of 4–7 W.

To investigate the impact of focused and defocused laser scanning on LIG's microstructure, scanning electron microscopy (SEM) characterization is adopted. DF-LIG and F-LIG exhibit obviously different surface morphologies, as the higher energy density in focused-laser pulse facilitates the photoetching effect, thus leading to deep and narrow gullies on F-LIG (Figures 2d and S17). In contrast, defocused-laser contributes to a broader range but weaker photoetching effect, resulting in a corrugated surface structure with shallow gullies and a more porous upper surface in DF-LIG (Figures 2e and S18). It can be demonstrated that the produced gases escapes across the whole surface in DF-LIG, while they preferentially pass through pores on the "cliff face" in F-LIG. The D peak, G peak and 2D peak located at 1340 cm⁻¹, 1567 cm⁻¹ and 2677 cm⁻¹ in the Raman spectra (Figure 2f₁) confirm the formation of LIG [31,32]. Both F-LIG and DF-LIG exhibit prominent D peaks,

primarily due to: (1) the formation of an amorphous structure during the conversion of PI to LIG, followed by the growth into a stacked graphitic structure containing 5-, 6-, and 7-membered rings [33]. (2) The presence of impurity elements N and O, derived from PI molecules and oxygen in the air [34]. Significantly, DF-LIG exhibits a smaller I_D/I_G ratio of ~0.67 compared to ~1.03 in F-LIG, indicating fewer defects and high-degree C- sp^3 to C- sp^2 transformation, which is consistent with the higher electrical conductivity of DF-LIG (**Figure 2f₂**). Laser-defocused scanning promotes the photothermal effect, which enables temperature rise and enhanced graphitization. Furthermore, the crystalline size (L_a) along the a-axis can be determined by the I_D/I_G ratio using the equation: $L_a = (2.4 \times 10^{-10}) \times \lambda_1^4 \times I_G/I_D)$ [35], where λ_1 is 532 nm (wavelength of Raman laser). As is shown in **Figures 2f₂** and **S19**, compared to F-LIG, both L_a and I_{2D}/I_G of DF-LIG are higher, suggesting the enlargement of the crystalline domains and reduced stacks. Simultaneously, DF-LIG exhibits noticeable narrowed and sharpened 2D band. These results imply that defocused laser pulse is beneficial to the expansion of graphene layers, resulting in improved quality.

The decomposition of PI and subsequent formation of LIG involves the bonds breaking (e.g. —O—and C—N) and bonds forming (e.g. C—C and C—O). Consequently, we conducted further analysis of the atomic binding state and elements content in F-LIG and DF-LIG using X-ray photoelectron spectroscopy (XPS) (Figures 2g and S20). The C—C bond content in DF-LIG (88.98%) is significantly higher than that in F-LIG (44.73%), while the content of C—O and C—O bonds is lower, indicating a higher degree of carbonization and graphitization in DF-LIG [36]. In PI molecule, the key bond energies of —O— and C—N are relatively low, causing them to preferentially dissociate under laser irradiation. Consequently, no C—N bonds were detected in the XPS results of F-LIG and DF-LIG. The increased C—O bonds in F-LIG may result from unreacted bonds in PI and the enhanced photoetching effect, which induces C dangling bonds that react with oxygen molecules in the air. Importantly, O=C—O bond, as an intermediate product (Figure S21), was detected in F-LIG, further indicating that DF-LIG underwent more complete reaction and resulting in better electrical conductivity.

Based on the aforementioned experimental investigation, laser-focused/defocused-dependent formation of LIG is summarized (Figure 2h): (1) When

laser is focused, energy is more concentrated with emerged higher energy density, resulting in a more pronounced photoetching effect. Consequently, the surface of PI rapidly forms a deep pit (steep cliff), where the photothermal effect causes heat to diffuse to surrounding areas, resulting in increased LIG thickness but insufficient crystalline domains. As a result, F-LIG exhibits more defects and lower electrical conductivity. (2) When laser is defocused, the enlargement of the laser-irradiated area improves energy distribution with lower energy density, resulting in decreased photoetching effect. Meanwhile, the photothermal effect is enhanced which lead to enhanced growth of crystalline domains, resulting in less defects and better electrical conductivity.

Electromagnetic modulation performance and mechanism of metasurfaces

To date, thinner materials with higher conductivity are typically preferred due to their greater potential in miniaturized shielding systems [37-39]. Consequently, we have adopted DF-LIG for subsequent exploration of EMI shielding performance. As depicted in **Figure 3a** and **b**, this metasurface shows continuous and dynamic regulation to electromagnetic waves. When rotation angle ranges from 0° (E//LIG) to 45° and from 135° to 180° , the metasurface is in the Off-state, shielding more than 60% of the waves. Conversely, when rotation angle ranges from 45° to 135° , the metasurface is in On-state, transmitting more than 60% of the waves. Further insights into the coefficients of transmission (T), reflection (R), and absorption (A) are displayed in **Figure S22**. With the angle increasing from 0° to 90° ($E \perp LIG$), A initially increases and then decreases under 8-26.5 GHz, while R generally shows a downward trend. Theses results reveal that the reflection of electromagnetic waves gradually reduce with the angle increase, which can be explained by the discontinuous conductive path and reduced secondary radiation (**Note S9**).

To explore the performance of this metasurface over a wide frequency band, the EMI SE was tested from 8–26.5 GHz (**Figure 3c₁–c₃**). This metasurface exhibits an inverted response to incident waves, demonstrating impressive On/Off switchable tunability across a broad frequency range (8–26.5 GHz). Laser power plays a critical role in the total EMI shielding SE (SE_T) in the On-state, with SE_T exhibiting a positive correlation with the laser power. By integrating the preceding experimental results from **Figure 2c**, it can be concluded that the

modulation performance is collectively influenced by the electrical conductivity and thickness of the LIG, providing a fundamental basis for future optimization of its functionality. Notably, the minimum achievable SE_T is only 0.441 dB at 9.85 GHz (laser power of 4 W), corresponding to a shielding efficiency of 9.66%. In contrast, the metasurface exhibits SE_T of 26.6 dB (shielding efficiency of 99.998%) upon Off-state at this frequency. This achievement is critical as it not only shows remarkable Off-state performance, but also addresses the challenge of suboptimal On-state performance in reported works, where the shielding efficiency is too high with the majority exceeding 50% (**Table S2**). To assess behavior under realistic conditions, we conducted oblique-incidence tests which demonstrate that the LIG metasurface can basically maintain the On/Off switchable functionality over incident angles from 0° to 80° (**Figure S31**).

Furthermore, a mechanistic study was adopted on absorption loss (SE_A) and reflection loss (SE_R) (**Figures S23** and **S24**). SE_T shows no obvious change with different frequency band under the Off-state, but SE_A and SE_R show opposite trend. With the frequency increasing, SE_R is reduced due to improved transmission performance and increased conductor loss of high frequency electromagnetic wave leads to enhanced reflection of incident waves; SE_A is overall increased because the distance between waveguide ports is fixed while incident wavelength is decreased, contributing to longer equivalent transmission path (**Note S10**). The results that highest SE_R at laser power of 6 W under Ku-band and K-band is consistent with the highest electric conductivity tendency of LIG, originated from improved conductivity inducing poorer impedance matching, thus leading to enhanced reflection of electromagnetic waves (**Note S11**).

Further investigation of EMI SE_T with varying LIG width (**Figure 3d**) and gap width (**Figure 3e**) revealed that a decrease in LIG width and an increase in gap width result in a lower SE_T . Simultaneously, both widths show minimal impact on SE_T upon Off-state with the average value is always higher 30 dB (**Figures S28** and **S29**). In **Figure 3f** and **Table S3**, we present a comparison of thickness and reconfigurability factor (r) between this work and reported works. Critically, pursuing for higher EMI SE usually means thicker material utilized. Thickness as such should be significantly concerned for considering application in future high-integrated electrons [40-43]. The factor of r is used as a measure of the On/Off

switchable performance and is calculated as following:

$$\begin{split} r &= SE_{on\%} \cdot f_{on} + SE_{off\%} \cdot f_{off} \\ f_{on} &= 1 - \frac{SE_{max\%} - 50\%}{SE_{max\%}} \\ f_{off} &= 1 - \frac{50\% - SE_{min\%}}{SE_{max\%}} \end{split}$$

where $SE_{on\%}$, $SE_{off\%}$, f_{on} , and f_{off} represents the shielding efficiency in the On-, Off-state and corresponding factor, respectively. $SE_{max\%}$ and $SE_{min\%}$ represents the maximum and minimum shielding efficiency in reported works on EMI shielding dynamic regulation. The middle value is adjusted from reported 20 dB [44] to 50% for evaluating On/Off switchable shielding performance. Our LIG based switch exhibits significant advantages, including reduced thickness and enhanced electromagnetic shielding modulation performance (a high r value of 9.66), compared to reported metal-free and metal-based materials (**Figure 3f**).

To explore the mechanism of modulated shielding performance, the simulation of electromagnetically induced currents on the metasurface was performed using CST Microwave Studio (Figure 3g₁ and h₁). The unit cell structure is simulated with periodic boundary conditions along the x and y axes, while Floquet port excitations are applied along the z direction (Figure S30). When the direction of the electric field is parallel (E//LIG) and perpendicular ($E \perp LIG$) to the strip-arranged graphene, respectively. The incident electromagnetic wave induces a current in the conductive LIG, generates a secondary electromagnetic wave that opposes the incident wave. The simulated results for current and voltage densities in Figure 3g₂ and g₃ (E//LIG) are significantly higher than those in Figure **3h₂** and **h₃** ($E \perp LIG$). The maximum current density is 5.19 A m⁻¹ (E//LIG) and 2.78 A m⁻¹ $(E \perp LIG)$, and the maximum voltage density is 5860 V m⁻¹ (E//LIG) and 1371 V m⁻¹ $(E \perp$ LIG). In the case of $E \perp \text{LIG}$, the discontinuous conductive path limits the induced current density and yoltage, leading to weaker secondary electromagnetic wave energy. Consequently, most of the incident waves are transmitted. Microscopically, the electrons in LIG oscillate back and forth in response to the change in the direction of the electric field, accompanied by secondary radiation. The wavelength of the incident waves (8-26.5 GHz) exceeds 1 cm, which is significantly larger than the gap between the strip-arranged LIG. When $E \perp$ LIG, the charged state of LIG changes only when the electric field direction alters, limiting the energy

acquisition of electrons (**Figure 3h₂** and **h₃**) and preventing outward radiation. Consequently, the incident energy is primarily converted into transmitted energy. When *E*//LIG, electrons move for extended periods with unchanged trajectories, thereby acquiring more energy. As a result, most of the incident energy is converted into electron kinetic energy (**Figure 3g₂** and **g₃**), and less energy is transmitted.

Metasurface based applications

To showcase the application prospects of the EMI shielding modulation, we design a series of scenarios utilizing the dynamic tunability of electromagnetic wave. As depicted in **Figure 4a**, the brightness of light bulb can be modulated by tuning stacking angle between metasurfaces. When the two metasurfaces are stacked perpendicularly, the majority of waves are blocked, and the induced current is too small to light the bulb. With the angle altered from 90° to 180°, the brightness gradually increases originating from enhanced current caused by less shielded waves. These variations in visible light output demonstrate its feasibility in smart electronics. Furthermore, its On/Off switchable function in wireless charging system is demonstrated (**Figure 4b**). The switching between charging and non-charging states can be easily achieved via rotating the metasurface by 90°. This experiment exhibits its potential in the real-time control of wireless system.

Significantly, we design a novel paradigm for data electromagnetic encryption. Figure 4c illustrates the application and near-field scanning test process. Tests were performed in a microwave anechoic chamber (Figure S32), where electromagnetic waves were emitted from the EM emission system, and a sliding-shaft scanning probe measured the field intensity behind each encoded unit. The unit with LIG//E is defined as "1", and the unit with LIG_is defined as "0" (Figure 4d₁). As such, the encoded surface enables a distinct patterned electromagnetic response through various permutations and combinations of "0/1". An encoded surface with 3×5 units was designed to encode all numbers (0–9) and letters (A–Z), where the arrangement of red cells enables visual patterning (Figure 4d₂ and d₃). Figure 4e exhibits the near-field scanning results, which clearly emerge the preset encoded information of "6" and "j". In addition, this strategy enables effective discrimination of visually ambiguous characters (Figure S33), including numerals vs. letters (e.g. "1" vs. "I" and "0" vs.

"O") and uppercase vs. lowercase letters (e.g. "J" vs. "j"). Moreover, a larger number of data points (such as color, transparency, depth, etc.) can be encoded in a single surface through different orientation of units from 0° to 90°, thus enabling, for instance, the encoding of a colored QR code storing substantial amounts of information. Especially in the process of encoding and decoding, the following factors jointly determine the final results: (1) the wavelength and direction of incident waves, (2) the arrangement design of the encoded surface, (3) the distance between surface and the scanning probe, (4) the corresponding information detected from the electromagnetic strength. Therefore, a one-to-one mapping of incident wave-encoded surface-decoded information can be established, thereby enabling the as-prepared metasurface to be applied in electromagnetic encryption and decryption of critical information.

CONCLUSION

This work presents smart LIG based metasurface designed for exceptional dynamic modulation of electromagnetic wave. Utilizing laser-induced ultrafast kinetics, this metasurface achieves rapid preparation, open-air processability, and micron-level thickness. Furthermore, laser-defocused, as compared to laser-focused scanning, results in a more complete reaction and improved electrical conductivity of LIG. Notably, this smart metasurface exhibits a superior shielding efficiency modulation range of 9.66–99.78% and a high reconfigurability factor of 19.31. The superior modulation capability is attributed to that stronger electron oscillation leads to improved secondary radiation in the opposite direction to the incident wave, when E//LIG (compared to $E \perp \text{LIG}$); as a result, the incident wave is effectively shielded. Finally, we demonstrate the metasurface's significant capability for information encoding and even encryption, highlighting broad applicability in commercial multifunctional and military electronic systems.

METHODS

Materials

Polyimide (PI) film with a thickness of 150 µm (Zhuzhou Times New Materials Technology Co., Ltd, China) was directly subjected to irradiation by an infrared laser platform

(ProtoLaser S, LPKF, Germany) in ambient condition to fabricate LIG patterns. The laser source generates infrared radiation of wavelength 1,064 nm. Before laser irradiation treatment, PI films were cleaned with ethanol to remove residues in factory production and cut into appropriate size (10 cm long and 2 cm wide). The pulse frequency of the laser is 200 kHz and the scanning speed is 15 mm/s. In order to investigate the structure and properties of LIG in focusing and defocusing laser mode processing, the focus height was set to 150 μm (on the surface of PI film) and 1500 μm (above the surface of PI film).

Characterization

The surface morphology of the sample was characterized using a scanning electron microscope (JSM-7610F Plus, JEOL, Japan). Raman spectra were characterized with a Raman spectrometer (dxr3, Thermo Fisher Scientific, USA). Square resistance and conductivity measurements of LIG prepared with different laser powers using a 4-Point Probes Resistivity Measurement System (RTS-8, four Probes Tech, China). Hyper-depth of field three-dimensional microscopic system (VHX-600E, Keyence, Norway) was adopted to capture high-definition images of surface topography for measuring the minimum line width and inter-line gap in Figures 1B, S3 and S4. XPS data were collected with a Scanning X-ray Microprobe (ESCALAB 250Xi, Thermo Fisher Scientific, USA). The dynamic degradation studies for the samples were carried out in air and N₂ atmosphere in a thermal analyser (STA 449 F3 Jupiter, Netzsch, Germany). PI were heated from ambient to 1673 K at the heating rate of 5 K/min. Electromagnetic interference shielding measurements of LIG metasurface were carried out in a rectangular waveguide using a vector network analyzer (N5225A, Keysight, 8–26.5 GHz). The measurements in the frequency range of 8.0–12.4 (X-band), 12.4-18.0 (Ku-band), and 18.0-26.5 (K-band) are adopted in corresponding type of waveguide. Based on the measured results, the coefficients of reflection (R), transmission (T), and absorption (4) can be determined by $R = |S_{II}|^2$, $T = |S_{2I}|^2$, and A = 1 - R - T. The reflection loss (SE_R) , absorption loss (SE_A) , and total shielding effectiveness (SE_T) can be determined as: $SE_R = -10\log(1 - R)$, $SE_A = -10\lg[T/(1 - R)]$, $SE_T = SE_R + SE_A$. The shielding efficiency can be calculated as: $[100 - 1/10^{\circ}(SE_T/10)] \times 100\%$. The near-field shielding effectiveness performance of LIG metasurface was carried out by a measurement system in

anechoic chamber. In this system, a scanning probe was employed to capture a near field signal leakage (magnetic field signal, *H*) from the covered shielding materials. One end of the micro-strip antenna and the scanning probe was connected to the port 1 and port 2 of VNA, respectively.

SUPPLEMENTARY DATA

Supplementary data are available at NSR online.

FUNDING

This work was supported by the National Natural Science Foundation of China (22279097, 62401413 and 92163208), the Key R&D Program of Hubei Province (2023BAB103), the Foundation of National Key Laboratory of Microwave Imaging Technology, Natural Science Foundation of Hubei Province (2025AFB038 and 2025AFD120), and the Fundamental Research Funds for the Central Universities (WUT: 2024IVA031).

AUTHOR CONTRIBUTIONS

P.C., Z.W., H.Z., D.W. and D.H. designed the experiments. P.C., X.Y., and Y.C. carried out the preparation of graphene based EMI shielding metasurface. X.Y., Y.C., W.Q. and H.F. conducted the characterization of structure, composition and morphology. X.Y. and Y.C. conducted the electromagnetic test. H.Z. and W.X. conducted CST simulation and analysis. P.C., X.Y. and R.L. collectively wrote the paper. All authors commented on the final manuscript.

Conflict of interest statement. None declared.

REFERENCES

- 1. Han M, Zhang D, Shuck CE *et al.* Electrochemically modulated interaction of MXenes with microwaves. *Nat Nanotechnol* 2023; **18**: 373-9.
- 2. Liu X, Li Y, Sun X *et al.* Off/On switchable smart electromagnetic interference shielding aerogel. *Matter* 2021; **4**: 1735-47.
- 3. Hao Y, Liu C, Keram R *et al.* Machine-learning assisted novel insulation layer stripping technology for upgrading the transparent emi shielding materials. *Nano Today* 2025; **61**: 102660.
- 4. Zhao Y, Tan S, Yu J *et al.* A rapidly assembled and camouflage-monitoring-protection integrated modular unit. *Adv Mater* 2025; **37**: 2412845.
- 5. Zhu R, Li Z, Deng G *et al.* Anisotropic magnetic liquid metal film for wearable wireless electromagnetic sensing and smart electromagnetic interference shielding. *Nano Energy* 2022; **92**: 106700.
- 6. Li Y, Tian X, Gao S-P *et al.* Reversible crumpling of 2D titanium carbide (MXene nanocoatings for stretchable electromagnetic shielding and wearable wireless communication. *Adv Funct Mater* 2020; **30**: 1907451.
- 7. Yuan W, Liu H, Wang X *et al.* Conductive MXene/melamine sponge combined with 3D printing resin base prepared as an electromagnetic interferences shielding switch. *Compos Part A-Appl S* 2021; **143**: 106238.
- 8. Zeng Z, Wang C, Siqueira G *et al.* Nanocellulose-MXene biomimetic aerogels with orientation-tunable electromagnetic interference shielding performance. *Adv Sci* 2020; 7: 2000979.
- 9. Wei Y, Hu C, Dai Z *et al.* Highly anisotropic MXene@wood composites for tunable electromagnetic interference shielding. *Compos Part A-Appl S* 2023; **168**: 107476.
- 10. Wang Y, Cheng X-D, Song W-L *et al.* Hydro-sensitive sandwich structures for self-tunable smart electromagnetic shielding. *Chem Eng J* 2018; **344**: 342-52.
- 11. Liao S-Y, Wang X-Y, Huang H-P *et al.* Intelligent shielding material based on VO₂ with tunable near-field and far-field electromagnetic response. *Chem Eng J* 2023; **464**: 142596.
- 12. Xia Z, Huang X, Liu J *et al.* Designing Ni₂MnSn heusler magnetic nanoprecipitate in copper alloy for increased strength and electromagnetic shielding. *Nat Commun* 2024; **15**: 10494.
- 13. Wang Z, Mao B, Wang Q *et al.* Ultrahigh conductive copper/large flake size graphene heterostructure thin-film with remarkable electromagnetic interference shielding effectiveness. *Small* 2018; **14**: 1704332.
- 14. Qian W, Fu H, Sun Y et al. Scalable assembly of high-quality graphene films via electrostatic-repulsion aligning. Adv Mater 2022; 34: 2206101.
- 15. Han J-H, Seok S-H, Jin YH *et al.* Robust 2D layered MXene matrix–boron carbide hybrid films for neutron radiation shielding. *Nat Commun* 2023; **14**: 6957.
- 16. Li X, Sheng X, Fang Y *et al.* Wearable janus-type film with integrated all-season active/passive thermal management, thermal camouflage, and ultra-high electromagnetic shielding efficiency tunable by origami process. *Adv Funct Mater* 2023; **33**: 2212776.

- 17. Shen B, Li Y, Yi D *et al.* Strong flexible polymer/graphene composite films with 3D saw-tooth folding for enhanced and tunable electromagnetic shielding. *Carbon* 2017; **113**: 55-62.
- 18. Liu Z, Wang G, Li P *et al.* Gradient in-plane oriented porous carbon inspired by fabrication of toasts for elegant EMI shielding performance. *Carbon* 2023; **207**: 136-43.
- 19. Yu C, Xie B, Yao X *et al.* Cabbage-like flexible fluororubber/carbon aerogel hybrids with negative poisson's ratios and excellent microwave absorption. *Matter* 2023; **6**: 4321-38.
- 20. Isari AA, Ghaffarkhah A, Hashemi SA *et al.* Structural design for EMI shielding: from underlying mechanisms to common pitfalls. *Adv Mater* 2024; **36**: 2310683.
- 21. Lee JS, Kim J-W, Lee JH *et al.* Flash-induced high-throughput porous graphene via synergistic photo-effects for electromagnetic interference shielding. *Nano Micro Lett* 2023; **15**: 191.
- 22. Lin J, Peng Z, Liu Y *et al.* Laser-induced porous graphene films from commercial polymers. *Nat Commun* 2014; **5**: 5714.
- 23. Inagaki M, Harada S, Sato T *et al.* Carbonization of polyimide film "Kapton". *Carbon* 1989; **27**: 253-7.
- 24. Schuepfer DB, Badaczewski F, Guerra-Castro JM *et al.* Assessing the structural properties of graphitic and non-graphitic carbons by Raman spectroscopy. *Carbon* 2020; **161**: 359-72.
- 25. Dreyfus RW. CN temperatures above laser ablated polyimide. *Appl Phys A* 1992; **55**: 335-9.
- 26. Cheng L, Yeung CS, Huang L et al. Flash healing of laser-induced graphene. Nat Commun 2024; 15: 2925.
- 27. Wang Z, Li P, Song R *et al.* High conductive graphene assembled films with porous micro-structure for freestanding and ultra-low power strain sensors. *Sci Bull* 2020; **65**: 1363-70.
- 28. Anderholm NC. Laser-generated stress waves. Appl Phys Lett 1970; 16: 113-5.
- 29. Phillips KC, Gandhi HH, Mazur E *et al.* Ultrafast laser processing of materials: a review. *Adv Opt Photonics* 2015; 7: 684-712.
- 30. Song Y, Li N, Han S *et al.* Macro-sized all-graphene 3D structures via layer-by-layer covalent growth for micro-to-macro inheritable electrical performances. *Adv Funct Mater* 2023; **33**: 2305191.
- 31. Chen Y, Lu X, Ma G *et al.* One-step laser-guided fabrication of 3D self-assembled graphene micro-rolls. *ACS Nano* 2025; **19**: 5769–80.
- 32. Chen Y, Guo Y, Xie B *et al.* Lightweight and drift-free magnetically actuated millirobots via asymmetric laser-induced graphene. *Nat Commun* 2024; **15**: 4334.
- Vashisth A, Kowalik M, Gerringer JC et al. Reaxff simulations of laser-induced graphene (LIG) formation for multifunctional polymer nanocomposites. ACS Appl Nano Mater 2020; 3: 1881-90.
- 34. Su R, Liang M, Yuan Y *et al.* High-performance sensing platform based on morphology/lattice collaborative control of femtosecond-laser-induced MXene-composited graphene. *Adv Sci* 2024; **11**: 2404889.

- 35. Cançado LG, Takai K, Enoki T *et al.* General equation for the determination of the crystallite size La of nanographite by Raman spectroscopy. *Appl Phys Lett* 2006; **88**: 163106.
- 36. Wang Z, Mao B, Zhao M *et al.* Ultrafast macroscopic assembly of high-strength graphene oxide membranes by implanting an interlaminar superhydrophilic aisle. *ACS Nano* 2022; **16**: 3934-42.
- 37. Pan F, Shi Y, Yang Y *et al.* Porifera-inspired lightweight, thin, wrinkle-resistance, and multifunctional MXene foam. *Adv Mater* 2024; **36**: 2311135.
- 38. Yang S, Lin Z, Wang X *et al.* Stretchable, transparent, and ultra-broadband terahertz shielding thin films based on wrinkled MXene architectures. *Nano Micro Lett* 2024; **16**: 165.
- 39. Qu L, Yang C, Tan S *et al.* A microwave absorption/infrared dual-band dynamic stealth regulator based on the carbon nanotube film and metamaterial. *Mater Today Nano* 2025; **29**: 100556.
- 40. Zhou X, Min P, Liu Y *et al.* Insulating electromagnetic-shielding silicone compound enables direct potting electronics. *Science* 2024; **385**: 1205-10.
- 41. Ren Y, Zhang F, Yan Z *et al.* Wearable bioelectronics based on emerging nanomaterials for telehealth applications. *Device* 2025; **3**: 100676.
- 42. Kashani H, Giroux M, Johnson I *et al.* Unprecedented electromagnetic interference shielding from three-dimensional Bi-continuous nanoporous graphene. *Matter* 2019; **1**: 1077-87.
- 43. Wan S, Chen Y, Huang C et al. Scalable ultrastrong MXene films with superior osteogenesis. *Nature* 2024; **634**: 1103-10.
- 44. Nan Z, Wei W, Lin Z et al. Flexible electromagnetic interference shields: Materials, structure and multifunctionalization. *Mater Sci Eng: R: Rep* 2024; **160**: 100823.

Figure Captions

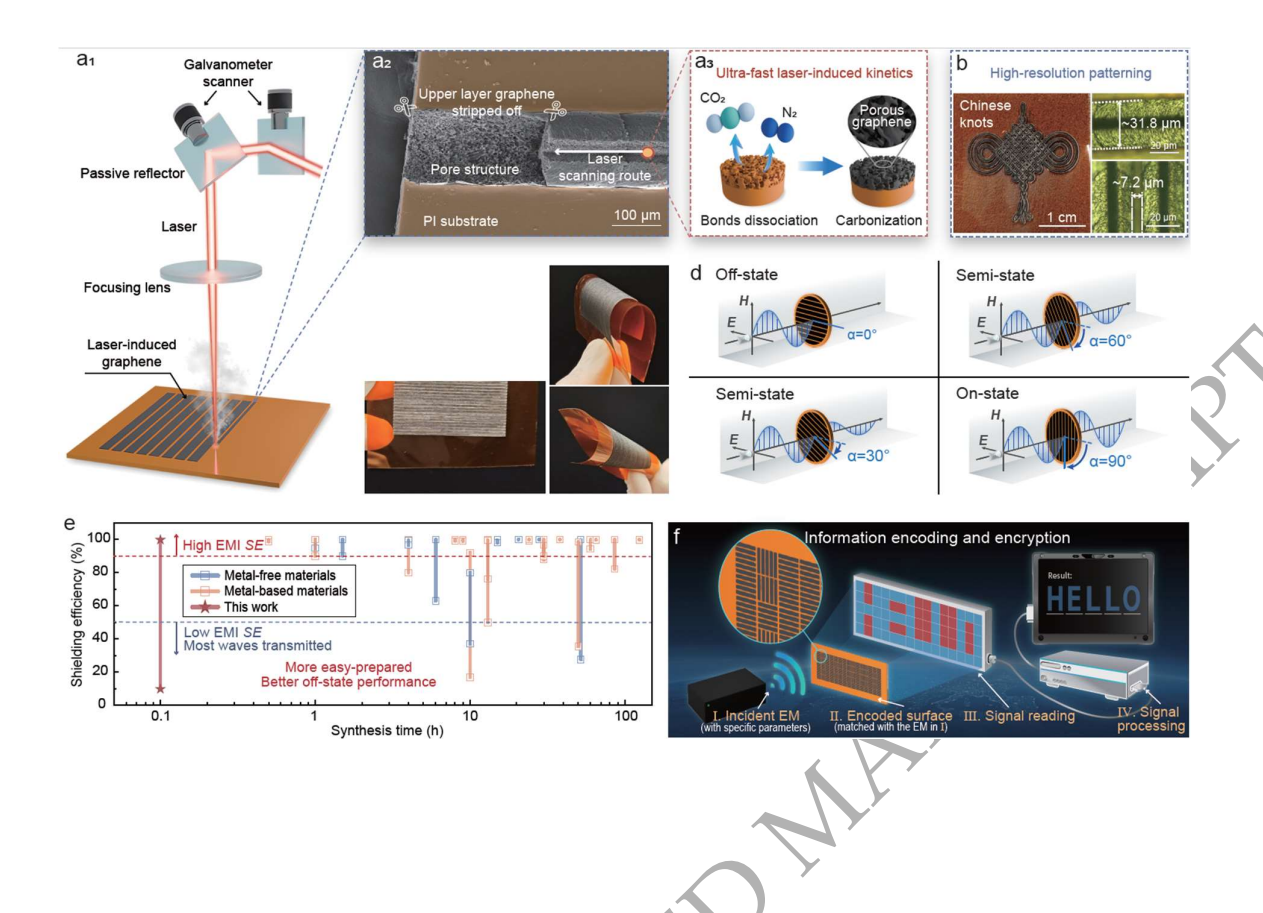


Figure 1. Fabrication, performance and application of the metasurface. (a) Characteristics of LIG technology. (a₁) Schematic of LIG technology applied on the polyimide (PI) film. (a₂) SEM image of LIG prepared by one-line laser scanning. (a₃) Schematic of laser-induced ultra-fast kinetics. (b) Photograph of Chinese-knot-shaped LIG, minimum line width and lines spacing. (c) Photograph of the LIG based metasurface. (d) Schematic illustration of the EMI shielding efficiency modulation. (e) Comparison of synthesis duration and shielding efficiency between reported works and this work. (f) Schematic showing the application of the metasurface on information encoding and encryption.

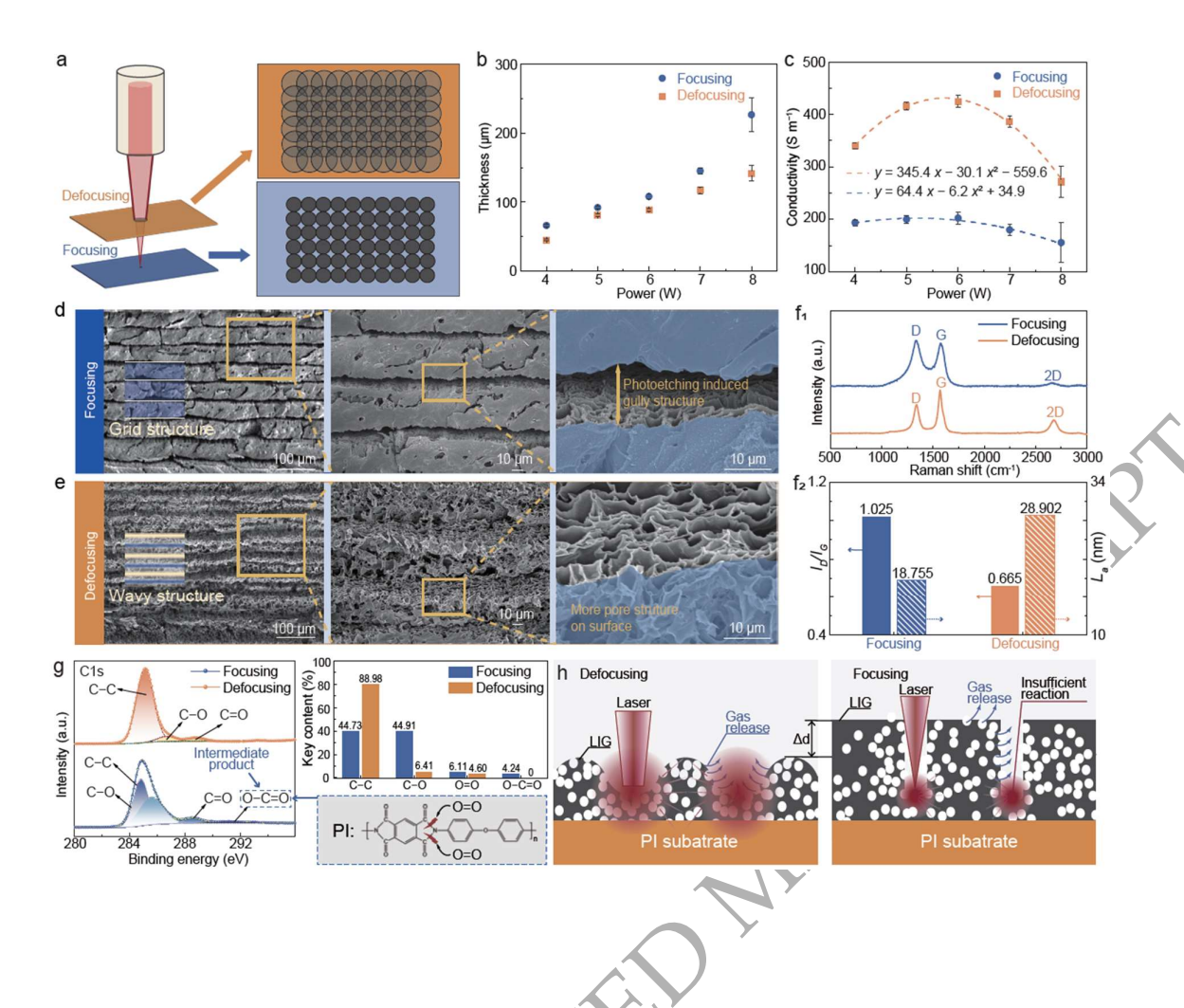


Figure 2. Comparison of laser-focused and laser-defocused prepared LIG. (a) Schematic illustration of the difference between laser-focused and laser-defocused scanning. (b) Thickness of F-LIG and DF-LIG fabricated under various laser powers. (c) Electrical conductivity of F-LIG and DF-LIG fabricated under various laser powers. (d and e) SEM images of F-LIG and DF-LIG surface at different magnification. (f) Raman spectra, I_D/I_G , and L_a of F-LIG and DF-LIG. (g) XPS spectra and key contents of F-LIG and DF-LIG. (h) Schematic illustration of the mechanism in F-LIG and DF-LIG fabrication.

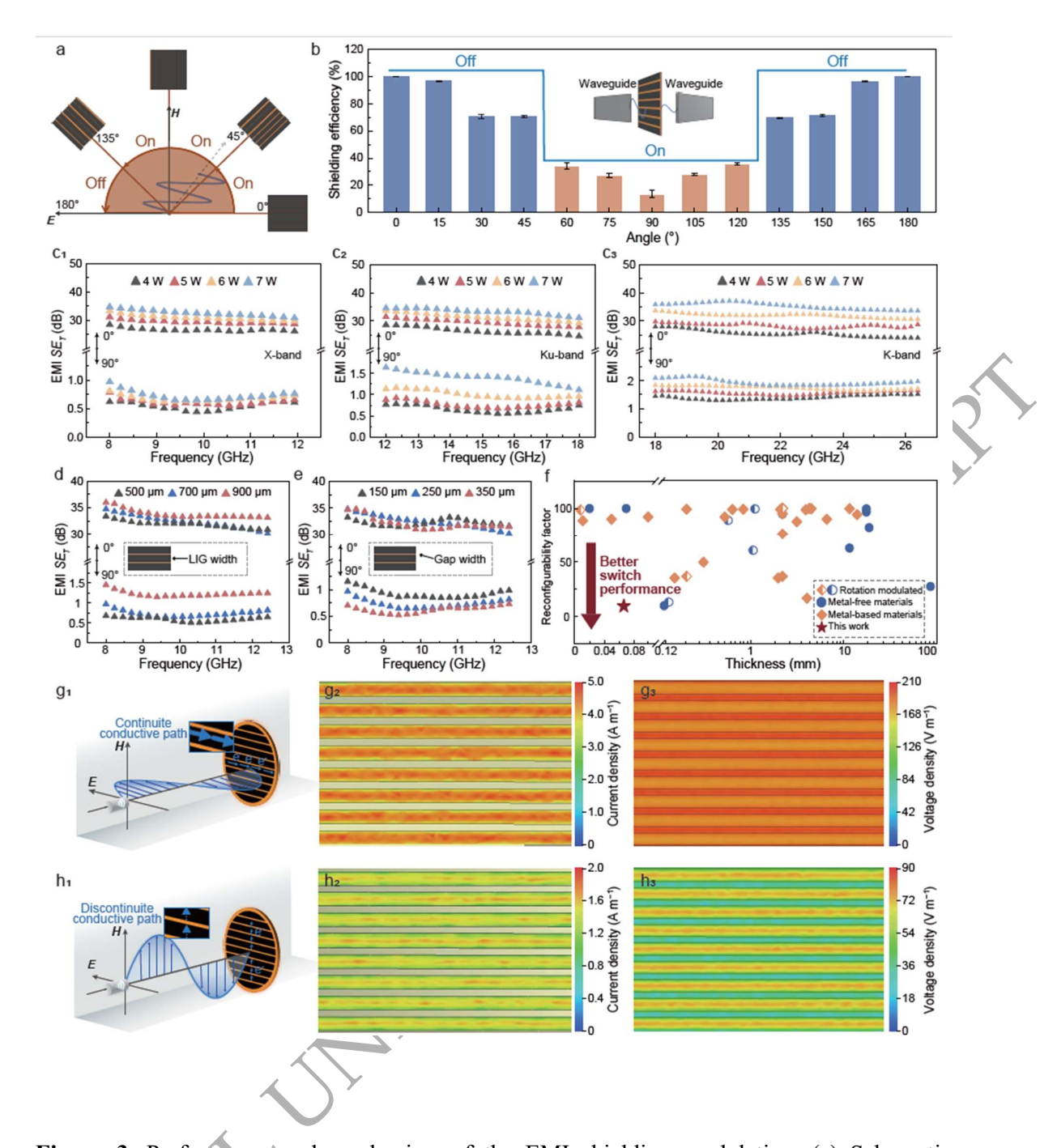


Figure 3. Performance and mechanism of the EMI shielding modulation. (a) Schematic showing the rotation process of the metasurface. (b) EMI shielding efficiency in various rotating angles at X-band. (c) EMI SE_T of at X-band, Ku-band and K-band. (d and e) EMI SE_T at X-band with various LIG width and gap width. (f) Comparison of the reconfigurability factor (r) between reported works and this work. (g and h) Schematic illustration of the EMI shielding modulation performance and current density and voltage density simulated by CST software.

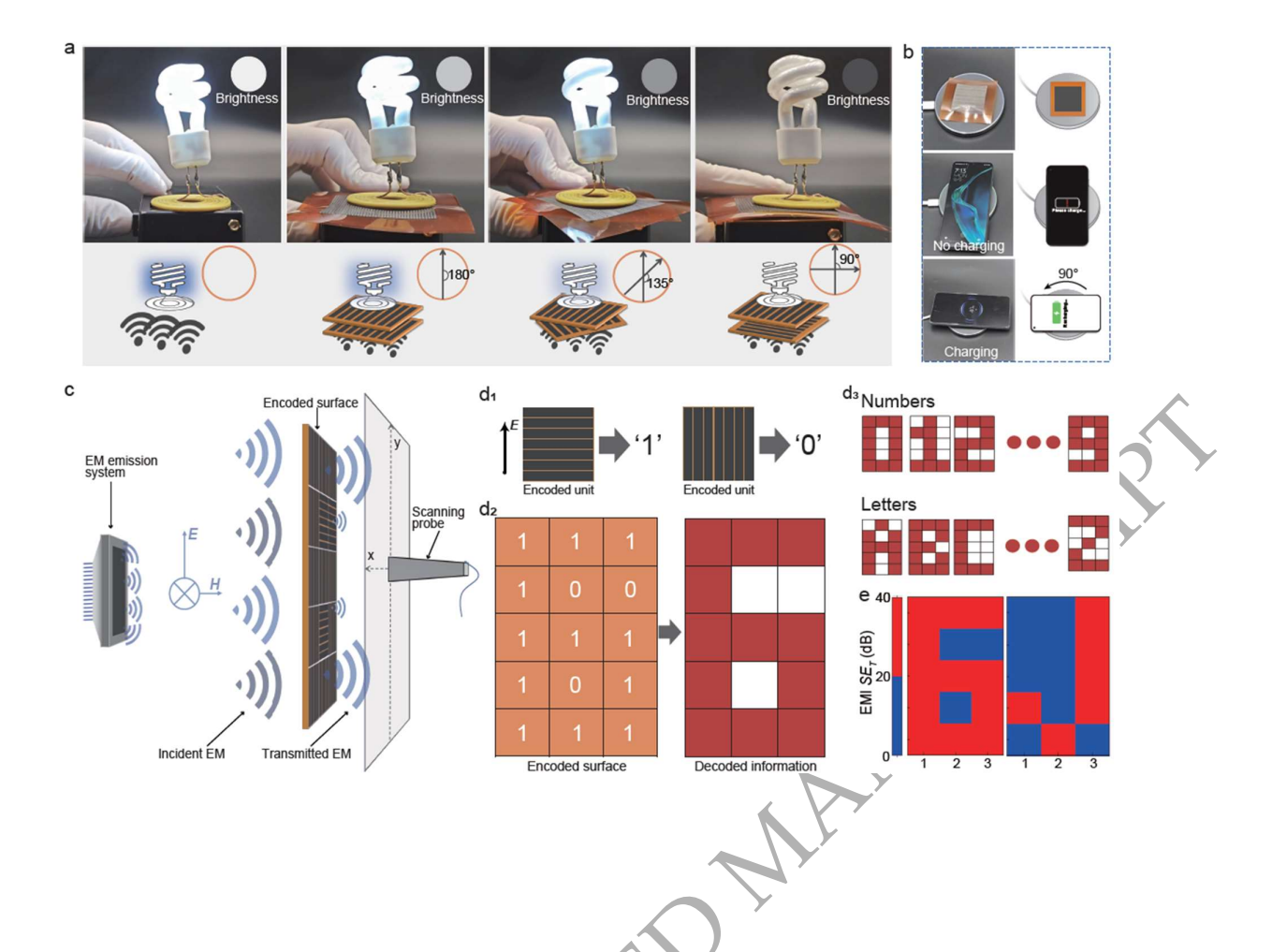


Figure 4. Application of the EMI shielding metasurface. (a) Light bulb brightness steerable phenomena controlled by two metasurfaces. (b) Wireless charging and no-charging controlled by the metasurface. (c) Schematic of electromagnetic near-field scanning test. (d₁–d₃) Schematic showing the application of information encoding. (d₁) Definition of "0" and "1" for coding. (d₂) Arrangement of coding units in number "6" encoding. (d₃) Schematic of encoding ability of all numbers and letters. (e) Electromagnetic near-field scanning test of the encoded surface.